ACS OMEGA

http://pubs.acs.org/journal/acsodf

Article

3D-Printed Complex Microstructures with a Self-Sacrificial Structure Enabled by Grayscale Polymerization and Ultrasonic Treatment

Yibo Liao, Wenhao Li, Ziheng Zhan, Huigao Duan, Peng Liu, Yiqin Chen, and Zhaolong Wang*

Cite This: *ACS Omega* 2021, 6, 18281−18288

Read Online

ACCESS | Metrics & More | Article Recommendations | Supporting Information

ABSTRACT: Complex three-dimensional (3D) microstructures are attracting more and more attention in many applications such as microelectromechanical systems, biomedical engineering, new materials, new energy, environmental protection, and wearable electronics. However, fabricating complex 3D microstructures by 3D printing techniques, especially those with long suspended structures, needs to introduce additional supporting structures, which are difficult to be removed. Here, we propose a simple method in which the supporting structures can be easily removed by optimizing their size and the grayscale value working with ultrasonic treatment in ethanol solution. The 3D microstructures and the supporting structures made of the same insoluble materials are fabricated simultaneously by using a projection microstereolithography system with a dynamic mask. The results demonstrate that the supporting structures play a key role in the fabrication of the long suspended structures while they can be easily removed. The removal time decreases with the increase in the height of the supporting microstructures, and the breaking force and shearing force of the supporting structures increase with the increase in their grayscale and the diameter. In addition, theory and the multiphysics simulation validate that the stress concentration at the top and the bottom of the supporting structures due to the cavitation from ultrasonic vibration dominates the removal of the supporting structures. Finally, a tree-like structure is precisely fabricated by using our method. The present study provides a new way for the removal of the supporting structures for 3D printed suspended microstructures.

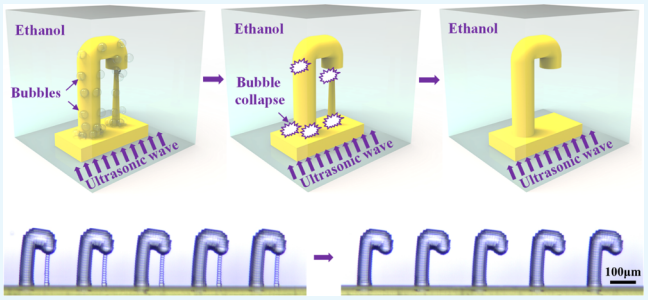

1. INTRODUCTION

As one of additive manufacturing techniques, the three-dimensional (3D) printing technique was proposed in the 19th century,[1] while the first 3D printer was proposed in the earlier 1980s. The 3D printing technique is based on a sequential layer-by-layer fabrication process,[2] which should cooperate with automated computer-assisted design (CAD) technology for fabricating highly complex 3D objects.[3] The merits of the 3D printing technique enable its growing applications in tissue engineering,[4,5] printed electronics,[6,7] composites,[8] and so on. In addition, the 3D printing technique is also applied to the fabrication of metamaterials,[9] microfluidic devices,[10] and microscale electromechanical systems.[11] Furthermore, the 3D printing technique has developed a lot in commercialization. For example, micro-fuel cells, ceramic parts, and artificial organs have been manufactured by the 3D printing technique.[12−16] With the fast development of the 3D printing technique, the sub-micronscale[17] and multi-material 3D printing technique is widely used.[18,19]

Complex 3D microstructures exhibit great potential for microelectromechanical (optical devices, microelectronics, sensors, and actuators), biomedical engineering (microfluidic devices, biochips, tissue engineering and drug delivery), new materials (metamaterials, composites, photonic crystals and functionally graded materials), new energy (solar batteries and micro-fuel batteries), and wearable electronics (electronic skins and pressure and strain sensors).[20−27] However, the existing silicon-based micromachining technologies mainly achieve simple 2D or 2.5D microstructures manufacturing, which is a significant challenge for the fabrication of complex 3D microstructures with suspended microstructures.[28] Furthermore, the equipment and mask of those techniques are expensive, the manufacturing time is quite long, and the available materials are not enough for variable applications. Therefore, manufacturing complex 3D microstructures (especially large area, high aspect ratio complex 3D composite microstructures) with high efficiency and low cost always troubles researchers all over the world.[29,30]

Microscale 3D printing techniques potentially solve those problems with the advantages of simple equipment, low cost, high efficiency, as well as a wide range of usable materials, no mask, and direct fabrication.[31,32] For these reasons, microscale

Received: April 24, 2021
Accepted: June 15, 2021
Published: July 8, 2021

ACS Publications

© 2021 The Authors. Published by American Chemical Society

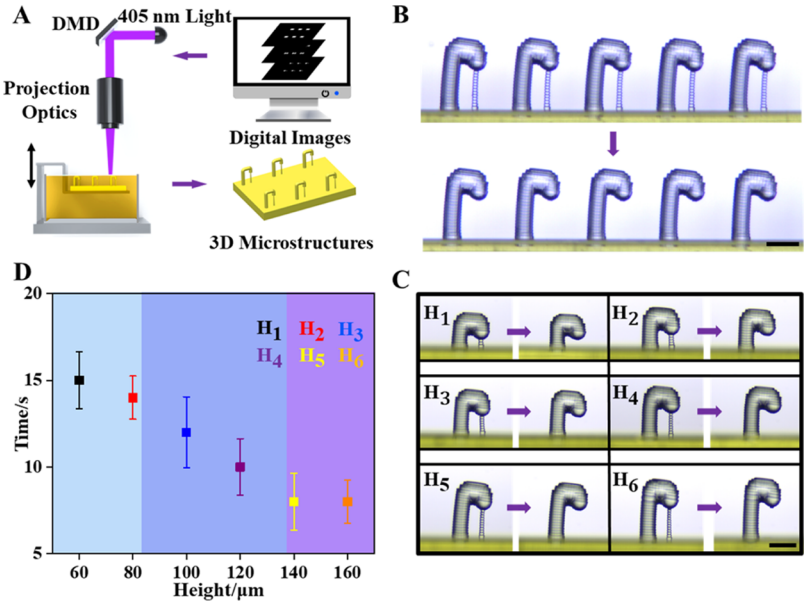

Figure 1. Complex 3D structures with a suspending microstructure fabricated by a PμSL-based 3D printing technique. (A) Schematic of the PμSL-based 3D printing system. (B) Removal of the sacrificed supporting microstructures, the height of the support structures was 160 μm. (C) Comparison of the removal of supporting structures with six different heights, which were 60, 80, 100, 120, 140, and 160 μm. (D) Time of ultrasonic treatment is affected by the height of the supporting structures. Scale bar is 100 μm for all the figures.

3D printing has begun to attract more and more interest in the manufacturing of complex 3D, high-aspect-ratio microstructures made of composite (multimaterial) materials. Based on different principles, materials, resolutions, and other factors, the high-resolution 3D printing technique can be roughly divided into the following groups: stereolithography, digital light processing (DLP), and two-photon polymerization.[33] However, there are various shortcomings for different 3D printing techniques considering their resolution and material compatibility.[34,35] What is more, the merits of the layer-by-layer fabrication manner also limit the applications of 3D printing for the fabrication of 3D complex microstructures with suspended branches.

Traditionally, 3D objects possessing overhanging structures need to introduce additional supporting structures. Those supporting structures should be easily removed after the fabrication process. However, it is impractical to complete the same process in complex 3D microstructures. One solution to this problem relies on the use of soluble support materials.[36,37] However, a layer made of a different material needs to be deposited and then removed in the etchant by such an approach which is tedious and of low efficiency. Another way to solve such a problem is by introducing supporting structures made of the same materials as the 3D microstructures, and the sacrificial layer can be removed by deep-UV at a 254 nm or a lower degree of polymerization from lower grayscale manufacturing.[28,38] However, those previous approaches are based on the principle that the materials are soluble, which is inapplicable to most of the printable materials in reality. In the present study, the sacrificial structure and the 3D complex microstructures made of the same insoluble materials are fabricated by a projection microstereolithography (PμSL)-based 3D printing technique[39−42] at the same time. Ultrasonic treatment in ethanol solution is employed for the removal of the sacrificial structures made of insoluble materials. The parameters affecting the perfect removal of the sacrificial supporting structure are also experimentally investigated and the underlying mechanisms are revealed by theory and the multiphysics simulation. The application of the present method is carried out for printing a tree-like microstructure with suspended branches, in which the sacrificial supporting structures are completely removed while the tree-like microstructure is well preserved. The present study promises a new potential strategy for the removal of sacrificial supporting structures for the fabrication of complex 3D structures with a suspending microstructure by employing a 3D printing technique.

2. RESULTS AND DISCUSSION

2.1. Fabrication of Complex 3D Microstructures with a Suspending Microstructure. The schematic of the PμSL-based 3D printing system (BMF S140) for the fabrication of the present complex 3D microstructures is shown in Figure 1A. The complex 3D microstructures model was firstly designed by a CAD software package. Then, the 3D CAD model was sliced into cross-sectional images at different altitudes, which would work as digital images. Each digital image was a thin layer of the 3D structure. Digital images were generated by a digital light processing (DLP) panel for our PμSL-based 3D printing system. The digital micromirror device (DMD) of the DLP panel with 1920 × 1080 pixels (the size of each pixel is 10 μm) is the most significant device to generate digital images. During the manufacturing process, one digital image was transformed and displayed on the DLP panel. The digital image was then delivered via the optical path and projected onto the ultraviolet (UV light, 405 nm) curable resin surface. The precise fabrication of the present 3D microstructures can be achieved by adjusting the UV light energy of the 3D printer (Figure S1A) and the grayscale value (0−255) of the image (Figure S1B). In the present study, polyurethane acrylate (PUA) was employed as the monomer, TPO-819 acted as the photoinitiator, and Sudan I was chosen as the UV photoabsorber (Figure S2A). The UV light with the shape of a digital image was projected onto the liquid resin surface for polymerization. The minimum thickness of each layer was 2 μm for our 3D printing system. Meanwhile, the curve of the curing depth versus light intensity is shown in

https://doi.org/10.1021/acsomega.1c02177
ACS Omega 2021, 6, 18281−18288

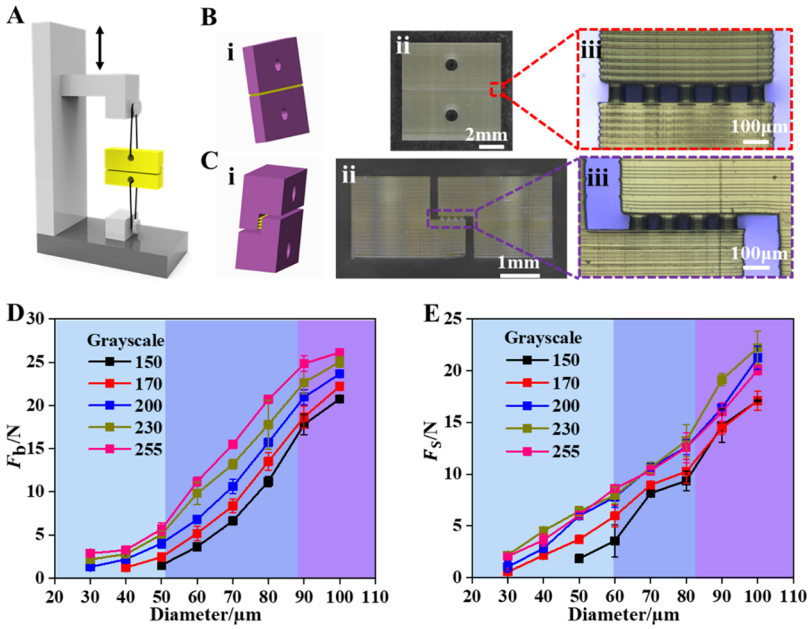

Figure 2. Effect of diameter and grayscale on breaking force (F_b) and shearing force (F_s) of the supporting structures, respectively. (A) Schematic of the experimental measurement of the forces. (B,C) Schematic and pictures for the samples of breaking force and shearing force tests, respectively. (i) 3D model for the tests, (ii) manufacturer's sample, (iii) enlarged section of the microstructures. (D) Effect of grayscale on F_b of the supporting structures with different diameters. (E) Effect of grayscale on F_s of the supporting structures with different diameters.

Figure S2B. The printing platform moved down with the cured product to print the next layer after curing the present one. This process was repeated until all digital images were projected. In this work, I_0 for a white digital image (grayscale value was set to 255) was 525 mW/cm^2 (setting value was 40). The curing time of those 3D microstructures was 0.2 s and the thickness of every layer was 2 μm.

Figure 1B demonstrates that the samples with the supporting microstructures (height was 160 μm) can be precisely manufactured by the PμSL printing system. A comparison of the upper figure and the bottom one in Figure 1B indicates that the 3D objects (the diameter of the main structure was 50 μm with an 80 μm long suspending microstructure) were well-preserved, while the sacrificed supporting structures of those 3D objects were almost completely removed after ultrasonic treatment for tens of seconds. Then, different 3D objects with six different heights but the same diameter (10 and 20 μm for their top and root) of supporting structures were fabricated, and the heights of the supporting structures were 60, 80, 100, 120, 140, and 160 μm, respectively, as shown in Figure 1C. However, the lengths of the overhung microstructures and the height of the "lamp" were the same. The results demonstrate that the supporting microstructures can be removed with the 3D objects well preserved, but the ultrasonic treatment time was different for different heights of the supporting microstructures. It can be observed from Figure 1D that the time of ultrasonic treatment decreased with the increase of the height of the supporting structures. The longest and the shortest time of the ultrasonic treatment were about 15 and 8 s for the height varied in the range of 60−160 μm, respectively.

2.2. Parameters Affecting the Removal of the Self-Sacrificial Structures. The parameters affecting the removal of the supporting microstructures were experimentally studied, as schematically shown in Figure 2A. The breaking force (F_b) and shearing force (F_s) of the samples were tested by an electronic tensile testing machine (ZQ-990A). Samples for investigating the effects of the diameter and grayscale on F_b and F_s of the supporting structures are respectively shown in Figure 2B,C with 3D models on the left while the pictures of the samples are on the right. It can be seen that both kinds of samples contained upper and bottom plates with micro-rods in between acting as supporting microstructures, as shown in Figure 2B-ii,C-ii. To reduce the errors of the experimental tests, there were 200 micro-rods for each sample to average the force (Figure 2B-iii,C-iii). In this section, I_0 for a white digital image was set as a constant, which was 525 mW/cm^2.

The grayscale value for printing those micro-rods varied from 150 to 255 to study its effect on the breaking force of the micro-rods. The curing time of those micro-rods was 0.2 s and the thickness of every layer during the printing process was 2 μm. In addition, the diameters of the micro-rods representing the supporting microstructures varied in the range of 30−100 μm to investigate the effect of the diameter of micro-rods on their breaking force. As shown in Figure 2D, F_b increased slowly with the increase of the diameters of the micro-rods in the region of 30−50 μm, for which the step of the breaking forces was in the range of 1−2 N for increasing the diameter by 10 μm. Then, a fast linear increase was observed when the diameters were in the range of 50−90 μm. Finally, the gradient became similar to that in the range of 30−50 μm. What is more, the breaking force increased with the increase of the grayscale value for printing those micro-rods, indicating that a higher intensity of the UV light could better solidify the resin at the interface between two adjacent layers during the printing process.

The experimental study of the shearing force of micro-rods was carried out, and the results are shown in Figure 2E. Similarly, I_0 for a white digital image was set to 525 mW/cm^2, while the grayscale value for printing micro-rods varied in the range of 150−255. Slightly different from the trend of the breaking force, F_s was almost linear to the diameter of the micro-rods with a diameter varying in the range of 30−80 μm. Then, F_s increased slightly faster with the increase of the micro-rods' diameter in the

https://doi.org/10.1021/acsomega.1c02177
ACS Omega 2021, 6, 18281−18288

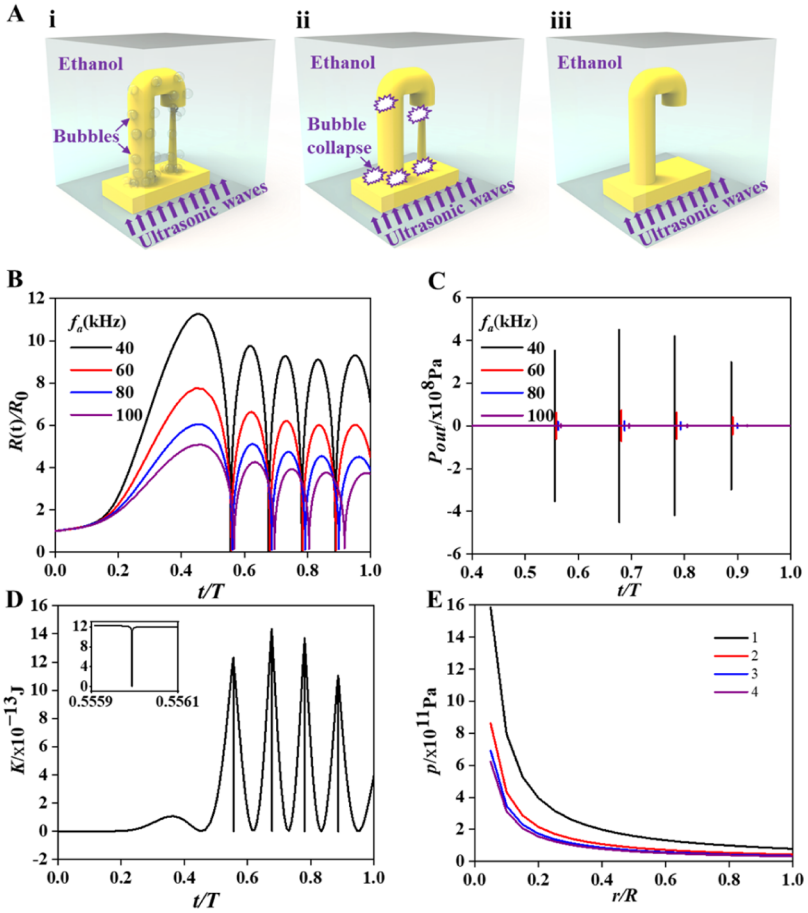

Figure 3. Cavitation theory for ultrasonic vibration. (A) Schematic of the cavitation process, (i,ii) process of growth and collapse of bubbles, (iii) supporting structures will be removed. (B) Effect of ultrasonic frequency (f_a) on the maximum radius of the bubble. (C) Effect of f_a on the pressure outside the bubble (p_{out}). (D) Total kinetic energy (K) of gas in a bubble during the cavitation process. (E) Value of shock wave (p) when the bubble collapses.

range of 80−100 μm. More interestingly, it could be observed that F_s was similar when the grayscale value ranged from 200 to 255, indicating that there was no difference in the solidification of the resin within each layer. F_s increased with the increase of the grayscale value when the grayscale value ranged from 150 to 200 as shown in Figure 2E, demonstrating that the solidification of the resin was not well done, and enhancing the UV light intensity could strengthen the micro-rods. It could also be concluded from Figure 2E that F_s increased with the increase of the diameter of the micro-rods. These experimental results validate that the diameter of the supporting microstructures is the most important factor affecting the mechanical properties of the supporting structures, although the changing grayscale value also makes a small difference in the mechanical properties of the supporting structures.

2.3. Underlying Mechanisms of the Removal of the Supporting Structures. The cavitation theory for ultrasonic vibration was proposed in previous studies,[43,44] which is used to explain the results in the present investigation. It is demonstrated in Figure 3A-i that there are many tiny bubbles at the interface of the liquid and the solid structures first. Then, these tiny bubbles quickly grow up at the negative pressure zones because of the ultrasound waves (Figure 3A-i), and they will collapse at the positive pressure zones with the longitudinal spread of ultrasound waves (Figure 3A-ii). Therefore, bubbles are compressed and stretched alternately under positive and negative pressures from the ultrasonic vibration. The huge pressure change at the surface of the supporting structures will break them up (Figure 3A-iii). The supporting structures will be almost completely removed after ultrasonic treatment for tens of seconds. Based on the cavitation theory (Supporting Information S3), it can be found that there are several cavitation bubbles generated during a single cycle; the maximum radius of the bubble decreases with the increase of the ultrasonic frequency (f_a) (Figure 3B). The value of pressure outside the bubble, p_{out}, during the cavitation process is shown in Figure 3C. It can be found that p_{out} decreases with the increase of f_a. f_a is 40 kHz for the present ultrasonic machine. Meanwhile, the effect of sound pressure amplitude, p_a, on the cavitation process is analyzed (Figure S3). The total kinetic energy (K) of gas in a bubble changes sharply with the growth and collapse of bubbles (Figure 3D). When bubbles are broken down after the compression, it will produce a tremendous pressure drop instantaneously (Figure 3E); such a vast pressure variation will certainly produce violent destruction of the supporting structures. Besides, it could be demonstrated that the value of p decreased with the increase of the distance to the bubble center as shown in Figure 3E.

Furthermore, the stress distribution within the micro-structures is numerically studied to reveal the underlying mechanisms of the removal of the sacrificed supporting structures. A cantilever beam is chosen to simplify the

https://doi.org/10.1021/acsomega.1c02177
ACS Omega 2021, 6, 18281−18288

microstructures in the calculation (Figure 4A), while the removal process is divided into two steps, which are (1) both the ends are fixed at the beginning (Figure 4B-i), (2) the bottom end is free while the other end contacts with the "street lamp" (Figure 4B-ii) or (2) the bottom end is fixed and the top is disconnected from the "street lamp" (Figure 4B-iii). The parameters of the microstructures are set as follows unless indicated otherwise: the diameter of the "street lamp" is 50 μm, the diameters of the supporting structure are 10 and 20 μm for its top and root, respectively. The height of the supporting structure varies in the range of 60−160 μm. The elastic modulus of material after 3D printing is 3.8 GPa, which is used in the calculation.

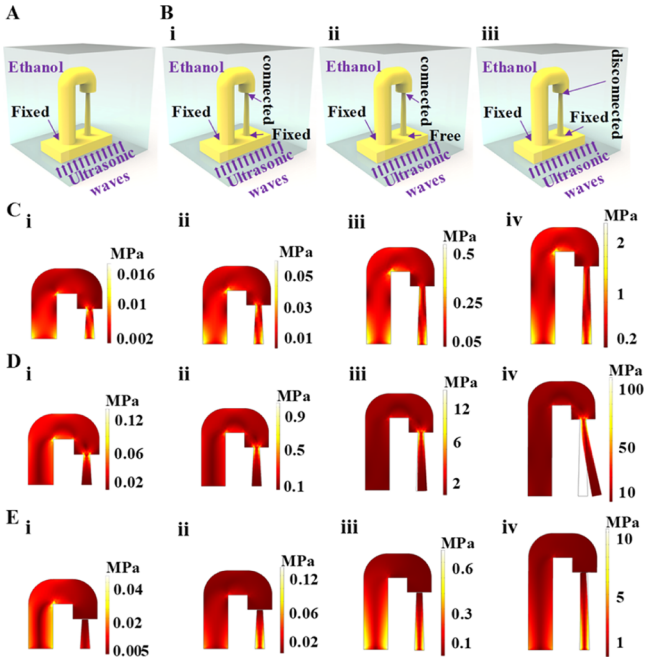

Figure 4. Underlying mechanisms for the removal of the supporting structures are affected by their height. (A) Schematic of the calculation model. (B) Different structures for the calculation, (i) both the ends of the supporting structure are fixed, (ii) bottom of the supporting structure is free while the top of it is fixed, (iii) bottom of the supporting structure is fixed while the top of it is free. (C) Stress distribution within the supporting structure with different heights with two ends fixed. (D) Stress distribution within the supporting structures with different heights with a free bottom end. (E) Stress distribution within the supporting structures with different heights with a free top. The diameter of the "street lamp" is 50 μm, the diameters of the supporting structure are 10 and 20 μm for its top and root, respectively, the heights of the supporting structures are set as (I) 60, (II) 80, (III) 120, and (IV) 160 μm.

The sound pressure distribution within ethanol is shown in Movie S1. The stress distribution within the microstructures is demonstrated in Figure 4C−E. It can be seen that the maximum stress in the microstructures increases with the increase of the supporting structures' height, indicating that it is easier to remove the higher supporting structures, which can be validated by the results shown in Figure 1. Specifically, the highest stress appears at the two ends of the supporting structures at first (Figure 4C and Movie S2), leading to the connection between the ends and the main structure being broken first. Then, the calculation for models with supporting structures free at the top and bottom is carried out, and the results are shown in Figure 4D,E, respectively. It can be seen from both sets of figures that the maximum stress appears at the remaining fixed end of the supporting structures, leading to the supporting structures being removed, while the "street lamp" can be well preserved with ultrasonic vibration in ethanol. In addition, the underlying mechanisms for the removal of the supporting structures affected by the grayscale (Figure S4) and diameter (Figure S5) are studied. It can be seen that reducing the grayscale value and diameter is also helpful in the removal of the supporting microstructures.

2.4. Fabrication of a Tree-like Complex 3D Structure.

To apply the results in the present study, a tree-like complex 3D structure was printed by the PμSL-based 3D printing system enabled with sacrificed supporting microstructures, as shown in Figure 5. As can be seen from the top and side views, respectively, demonstrated in Figure 5A,B, there were tree-like branches for such a complex structure, and the printing of such a structure must accord with the supporting microstructures. The diameter of tree branches ranged from 50 to 120 μm and the diameter of the supporting structures ranged from 10 to 20 μm. The thickness of each printing layer was 2 μm. In addition, the curing times for the supporting microstructures and tree-like complex structure were 0.2 and 0.5 s, respectively.

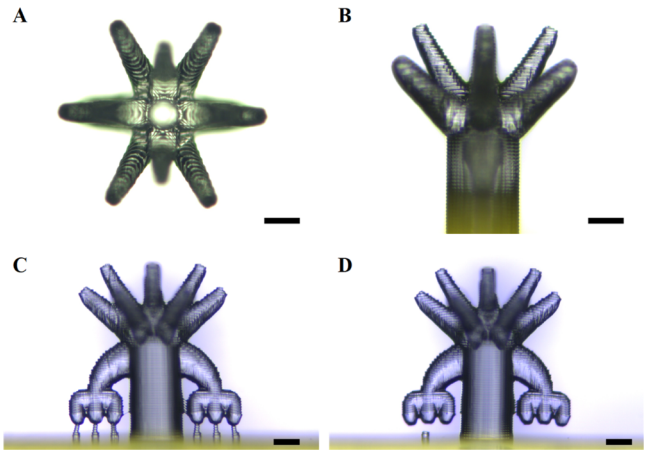

Figure 5. Tree-like complex 3D structure fabrication enabled by sacrificed supporting microstructures. (A) Top view of a tree-like complex 3D structure. (B) Side view of the tree-like complex 3D structure. (C) Optical microscope image of a tree-like complex 3D structure with supporting structures. (D) The tree after ultrasonic treatment for 30 s. Scale bar is 100 μm.

It can be seen from Figure 5C that the tree-like complex structure can be precisely printed with the setting parameters mentioned above. Such a result revealed that the supporting microstructures played a key role in the fabrication of such kinds of complex 3D structures with large suspending branches. The removal of the supporting microstructures assisted with ultrasonic treatment was shown in Figure 5D. It can be seen from Figure 5D that the tree-like structure was well preserved while the supporting microstructures had been removed. The tree-like complex structure was fabricated with a longer curing time of 0.5 s compared with the curing time of 0.2 s for supporting structures, leading to a fact that the tree-like structure had better mechanical properties than those of the supporting structures. Therefore, it was easier to remove the supporting microstructures than the tree-like structure when treated by ultrasound. These experimental results clearly demonstrate that

https://doi.org/10.1021/acsomega.1c02177
ACS Omega 2021, 6, 18281−18288

the present conclusions can be well applied to the fabrication of complex 3D microstructures by the 3D printing technique.

3. CONCLUSIONS

In summary, the removal of supporting microstructures enabled by ultrasonic treatment is experimentally, theoretically, and numerically studied. The results indicate that the time of ultrasonic treatment for removal of supporting microstructures depends on the height, diameter, and printing parameters. The ultrasonic treatment time decreases with the increase of the height of the supporting microstructures, whereas it increases with the increase of their diameter. In addition, the ultrasonic treatment time also increases with the increase of the grayscale value of the 3D printing system. The underlying mechanisms are revealed by cavitation theory for ultrasonic vibration and the numerical calculations. The stress concentration from cavitation at the top and bottom of the supporting microstructures mainly contributes to their fracture, and the trend of the stress concentration is similar to the parameters that affect the ultrasonic treatment time. Moreover, the breaking force and shearing force of the printed microstructures are also experimentally studied to provide solid foundations for the removal of the sacrificed supporting structures. Most importantly, a tree-like complex 3D microstructure with suspended branches was printed by a PμSL-based 3D printing technique enabled by the sacrificed supporting microstructures. The well-preserved tree-like structure with complete removal of the supporting microstructures clearly validates that the present study opens a new gate for the fabrication of the same kind of complex microstructures with the 3D printing technique by using sacrificed supporting structures treated by ultrasound.

4. EXPERIMENTAL SECTION

4.1. Fabrication of Complex Structures with Supporting Structures. The complex 3D structures with the suspended structure and supporting structures were fabricated simultaneously by a PμSL-based 3D printing system (S140, BMF Material Technology Inc., China). We first designed the complex 3D microstructures model by a CAD software. Then, the 3D CAD model was sliced into cross-sectional images at different altitudes, which will work as digital images. During the manufacturing process, one digital image was first transformed on the DMD with 1920 × 1080 pixels (the size of each pixel is 10 μm). The digital image was then projected onto the ultraviolet (UV light, 405 nm) curable resin surface. The UV resin is made of the monomer (PUA), photoinitiator (TPO 819), and photoabsorber (Sudan I), which is insoluble after polymerization. Each digital image was a thin layer of the 3D structure. This process will be repeated until all digital images were projected. The curing time was set as 0.2 s and the thickness of every layer was 2 μm.

4.2. Numerical Method. The analysis is carried out based on the theoretical calculation and the multiphysics simulation. The theoretical calculation of the cavitation process of bubbles was achieved by MATLAB, while the pressure distribution within the 3D microstructures is analyzed through COMSOL Multiphysics software.

4.3. Removal of the Supporting Microstructures. We first fabricated the samples with the supporting structures (height was 160 μm). The supporting structures can be completely removed after ultrasonic treatment (DS-020S, Pinchuang Technology Inc., China) in ethanol for tens of seconds. Then, different objects with six different heights (60, 80, 100, 120, 140, and 160 μm) but the same diameter (10 and 20 μm for their top and root) of supporting structures were fabricated. These supporting structures with six different heights were completely removed after ultrasonic treatment in ethanol similarly.

4.4. Measurement of the Breaking Force and Shearing Force. We fabricated the samples containing upper and bottom plates with 200 micro-rods in between acting as supporting microstructures. We first tested the F_b and F_s of the samples with different diameters by an electronic tensile testing machine (model ZQ-990A, Dongguan, China). Afterward, the F_b and F_s of the supporting structures with different grayscale values that varied from 150 to 255 were tested

■ ASSOCIATED CONTENT

Supporting Information

The Supporting Information is available free of charge at https://pubs.acs.org/doi/10.1021/acsomega.1c02177.

Sound pressure distribution within ethanol (MP4)

Stress distribution within the microstructures when both the ends are fixed (MP4)

Detailed parameters of the 3D printing system; composition of the resin and its penetration depth; theoretical study of ultrasonic cavitation and simulation analysis of its influencing factors; stress distribution within the supporting structures with different grayscale values and diameters; and underlying mechanisms for the removal of the supporting structures affected by the diameter (PDF)

■ AUTHOR INFORMATION

Corresponding Author

Zhaolong Wang − *National Research Center for High-Efficiency Grinding, College of Mechanical and Vehicle Engineering, Hunan University, Changsha 410082, PR China;* orcid.org/0000-0003-2967-4546; Email: zhaolongwang@hnu.edu.cn

Authors

Yibo Liao − *National Research Center for High-Efficiency Grinding, College of Mechanical and Vehicle Engineering, Hunan University, Changsha 410082, PR China*

Wenhao Li − *National Research Center for High-Efficiency Grinding, College of Mechanical and Vehicle Engineering, Hunan University, Changsha 410082, PR China*

Ziheng Zhan − *National Research Center for High-Efficiency Grinding, College of Mechanical and Vehicle Engineering, Hunan University, Changsha 410082, PR China*

Huigao Duan − *National Research Center for High-Efficiency Grinding, College of Mechanical and Vehicle Engineering, Hunan University, Changsha 410082, PR China;* orcid.org/0000-0002-7016-6343

Peng Liu − *National Research Center for High-Efficiency Grinding, College of Mechanical and Vehicle Engineering, Hunan University, Changsha 410082, PR China*

Yiqin Chen − *National Research Center for High-Efficiency Grinding, College of Mechanical and Vehicle Engineering, Hunan University, Changsha 410082, PR China;* orcid.org/0000-0003-4635-0666

Complete contact information is available at: https://pubs.acs.org/10.1021/acsomega.1c02177

https://doi.org/10.1021/acsomega.1c02177
ACS Omega 2021, 6, 18281−18288

Notes

The authors declare no competing financial interest.

■ ACKNOWLEDGMENTS

Z.W. and Y.L. conceived the project, designed the experiments, and carried out the experimental work. W.L. did the simulation, Z.Z. theoretically analyzed the results, Y.C. and P.L. helped to design the project, Y.L., H.D., and Z.W. analyzed the data and wrote the manuscript. Z.W. supervised the whole project. All the authors discussed the results and commented on the manuscript. This work was supported by Key-Area Research and Development Program of Guangdong Province (2020B090923003) and the National Natural Science Foundation of China (52006056). The project was also supported in part by Science and Technology Bureau Foundation of Changsha City (kh1904005).

■ REFERENCES

(1) Schubert, C.; Van Langeveld, M. C.; Donoso, L. A. Innovations in 3D printing: a 3D overview from optics to organs. *Br. J. Ophthalmol.* **2014**, *98*, 159−161.

(2) Layani, M.; Wang, X.; Magdassi, S. Novel materials for 3D printing by photopolymerization. *Adv. Mater.* **2018**, *30*, 1706344.

(3) Bikas, H.; Stavropoulos, P.; Chryssolouris, G. Additive manufacturing methods and modelling approaches: a critical review. *Int. J. Adv. Des. Manuf. Technol.* **2016**, *83*, 389−405.

(4) Derby, B. Printing and prototyping of tissues and scaffolds. *Science* **2012**, *338*, 921−926.

(5) Hutmacher, D. W. Scaffolds in tissue engineering bone and cartilage. *Biomaterials* **2000**, *21*, 2529−2543.

(6) Kong, Y. L.; Tamargo, I. A.; Kim, H.; Johnson, B. N.; Gupta, M. K.; Koh, T.-W.; Chin, H.-A.; Steingart, D. A.; Rand, B. P.; McAlpine, M. C. 3D printed quantum dot light-emitting diodes. *Nano Lett.* **2014**, *14*, 7017−7023.

(7) Lewis, J. A.; Ahn, B. Y. Three-dimensional printed electronics. *Nature* **2015**, *518*, 42−43.

(8) Compton, B. G.; Lewis, J. A. 3D-printing of lightweight cellular composites. *Adv. Mater.* **2014**, *26*, 5930−5935.

(9) Wang, Q.; Jackson, J. A.; Ge, Q.; Hopkins, J. B.; Spadaccini, C. M.; Fang, N. X. Lightweight mechanical metamaterials with tunable negative thermal expansion. *Phys. Rev. Lett.* **2016**, *117*, 175901.

(10) van der Linden, P. J. E. M.; Popov, A. M.; Pontoni, D. Accurate and rapid 3D printing of microfluidic devices using wavelength selection on a DLP printer. *Lab Chip* **2020**, *20*, 4128−4140.

(11) Huang, J.; Zhou, J.; Luo, Y.; Yan, G.; Liu, Y.; Shen, Y.; Xu, Y.; Li, H.; Yan, L.; Zhang, G.; Fu, Y.; Duan, H. Wrinkle-Enabled Highly Stretchable Strain Sensors for Wide-Range Health Monitoring with a Big Data Cloud Platform. *ACS Appl. Mater. Interfaces* **2020**, *12*, 43009−43017.

(12) Sun, K.; Wei, T.-S.; Ahn, B. Y.; Seo, J. Y.; Dillon, S. J.; Lewis, J. A. 3D printing of interdigitated Li-Ion microbattery architectures. *Adv. Mater.* **2013**, *25*, 4539−4543.

(13) Wang, X. F.; Zou, B.; Li, L.; Xing, H. Y.; Huang, C. Z.; Wang, Y. S.; Shi, Z. Y.; Liu, J. K.; Yao, P.; Xue, K. Manufacturing of a ceramic groove part based on additive and subtractive technologies. *Ceram. Int.* **2020**, *47*, 740−747.

(14) Liu, K.; Zhou, C.; Chen, F.; Sun, H.; Zhang, K. Fabrication of complicated ceramic parts by gelcasting based on additive manufactured acetone-soluble plastic mold. *Ceram. Int.* **2020**, *46*, 25220−25229.

(15) Grigoryan, B.; Paulsen, S. J.; Corbett, D. C.; Sazer, D. W.; Fortin, C. L.; Zaita, A. J.; Greenfield, P. T.; Calafat, N. J.; Gounley, J. P.; Ta, A. H.; Johansson, F.; Randles, A.; Rosenkrantz, J. E.; Louis-Rosenberg, J. D.; Galie, P. A.; Stevens, K. R.; Miller, J. S. Multivascular networks and functional intravascular topologies within biocompatible hydrogels. *Science* **2019**, *364*, 458−464.

(16) Koffler, J.; Zhu, W.; Qu, X.; Platoshyn, O.; Dulin, J. N.; Brock, J.; Graham, L.; Lu, P.; Sakamoto, J.; Marsala, M.; Chen, S.; Tuszynski, M. H. Biomimetic 3D-printed scaffolds for spinal cord injury repair. *Nat. Med.* **2019**, *25*, 263−269.

(17) Saha, S. K.; Wang, D.; Nguyen, V. H.; Chang, Y.; Oakdale, J. S.; Chen, S.-C. Scalable submicrometer additive manufacturing. *Science* **2019**, *366*, 105−109.

(18) Zhu, M. Z.; Xie, M. Y.; Lu, X. M.; Okada, S.; Kawamura, S. A soft robotic finger with self-powered triboelectric curvature sensor based on multi-material 3D printing. *Nano Energy* **2020**, *73*, 104722.

(19) Rafiee, M.; Farahani, R. D.; Therriault, D. Multi-Material 3D and 4D Printing: A Survey. *Adv. Sci.* **2020**, *7*, 1902307.

(20) Kawata, S.; Sun, H.-B.; Tanaka, T.; Takada, K. Finer features for functional microdevices. *Nature* **2001**, *412*, 697−698.

(21) del Campo, A.; Arzt, E. Fabrication approaches for generating complex micro- and nanopatterns on polymeric surfaces. *Chem. Rev.* **2008**, *108*, 911−945.

(22) Armand, M.; Tarascon, J.-M. Building better batteries. *Nature* **2008**, *451*, 652−657.

(23) Xie, X.; Pu, H.; Sun, D.-W. Recent advances in nanofabrication techniques for SERS substrates and their applications in food safety analysis. *Crit. Rev. Food Sci. Nutr.* **2018**, *58*, 2800−2813.

(24) Xu, Q.; Lv, Y.; Dong, C.; Sreeprased, T. S.; Tian, A.; Zhang, H.; Tang, Y.; Yu, Z.; Li, N. Three-dimensional micro/nanoscale architectures: fabrication and applications. *Nanoscale* **2015**, *7*, 10883−10895.

(25) Jakus, A. E.; Secor, E. B.; Rutz, A. L.; Jordan, S. W.; Hersam, M. C.; Shah, R. N. Three-dimensional printing of high-content graphene scaffolds for electronic and biomedical applications. *ACS Nano* **2015**, *9*, 4636−4648.

(26) LaVan, D. A.; McGuire, T.; Langer, R. Small-scale systems for in vivo drug delivery. *Nat. Biotechnol.* **2003**, *21*, 1184−1191.

(27) Jones, N. Science in Three Dimensions: The Print Revolution. *Nature* **2012**, *487*, 22−23.

(28) Xia, C.; Fang, N. Fully three-dimensional microfabrication with a grayscale polymeric self-sacrificial structure. *J. Micromech. Microeng.* **2009**, *19*, 115029.

(29) Ahn, S. H.; Guo, L. J. Large-area roll-to-roll and roll-to-plate nanoimprint lithography: a step toward high-throughput application of continuous nanoimprinting. *ACS Nano* **2009**, *3*, 2304−2310.

(30) Zhang, Y.-L.; Chen, Q.-D.; Xia, H.; Sun, H.-B. Designable 3D nanofabrication by femtosecond laser direct writing. *Nano Today* **2010**, *5*, 435−448.

(31) Vaezi, M.; Seitz, H.; Yang, S. A review on 3D micro-additive manufacturing technologies. *Int. J. Adv. Des. Manuf. Technol.* **2013**, *67*, 1721−1754.

(32) Park, J.-U.; Hardy, M.; Kang, S. J.; Barton, K.; Adair, K.; Mukhopadhyay, D. K.; Lee, C. Y.; Strano, M. S.; Alleyne, A. G.; Georgiadis, J. G.; Ferreira, P. M.; Rogers, J. A. High-resolution electrohydrodynamic jet printing. *Nat. Mater.* **2007**, *6*, 782−789.

(33) Ge, Q.; Li, Z.; Wang, Z.; Kowsari, K.; Zhang, W.; He, X.; Zhou, J.; Fang, N. X. Projection micro stereolithography based 3D printing and its applications. *Int. J. Extreme Manuf.* **2020**, *2*, 022004.

(34) McHugh, K. J.; Nguyen, T. D.; Linehan, A. R.; Yang, D.; Behrens, A. M.; Rose, S.; Tochka, Z. L.; Tzeng, S. Y.; Norman, J. J.; Anselmo, A. C.; Xu, X.; Tomasic, S.; Taylor, M. A.; Lu, J.; Guarecuco, R.; Langer, R.; Jaklenec, A. Fabrication of fillable microparticles and other complex 3D microstructures. *Science* **2017**, *357*, 1138−1142.

(35) Stansbury, J. W.; Idacavage, M. J. 3D printing with polymers: Challenges among expanding options and opportunities. *Dent. Mater.* **2016**, *32*, 54−64.

(36) Bagolini, A.; Pakula, L.; Scholtes, T. L. M.; Pham, H. T. M.; French, P. J.; Sarro, P. M. Polyimide sacrificial layer and novel materials for post-processing surface micromachining. *J. Micromech. Microeng.* **2002**, *12*, 385−389.

(37) Linder, V.; Gates, B. D.; Ryan, D.; Parviz, B. A.; Whitesides, G. M. Water-soluble sacrificial layers for surface micromachining. *Small* **2005**, *1*, 730−736.

https://doi.org/10.1021/acsomega.1c02177
ACS Omega 2021, 6, 18281−18288

(38) Johnstone, R. W.; Foulds, I. G.; Parameswaran, M. Self-sacrificial surface micromachining using poly(methyl methacrylate). *J. Micromech. Microeng.* **2008**, *18*, 115012.
(39) Choi, J.-W.; Wicker, R.; Lee, S.-H.; Choi, K.-H.; Ha, C.-S.; Chung, I. Fabrication of 3D biocompatible/biodegradable microscaffolds using dynamic mask projection microstereolithography. *J. Mater. Process. Technol.* **2009**, *209*, 5494−5503.
(40) Chen, X.; Liu, W.; Dong, B.; Lee, J.; Ware, H. O. T.; Zhang, H. F.; Sun, C. High-speed 3D printing of millimeter size customized aspheric imaging lenses with sub 7 nm surface roughness. *Adv. Mater.* **2018**, *30*, 1705683.
(41) Zheng, X.; Smith, W.; Jackson, J.; Moran, B.; Cui, H.; Chen, D.; Ye, J.; Fang, N.; Rodriguez, N.; Weisgraber, T.; Spadaccini, C. M. Multiscale metallic metamaterials. *Nat. Mater.* **2016**, *15*, 1100−1106.
(42) Zheng, X.; Deotte, J.; Alonso, M. P.; Farquar, G. R.; Weisgraber, T. H.; Gemberling, S.; Lee, H.; Fang, N.; Spadaccini, C. M. Design and optimization of a light-emitting diode projection micro-stereolithography three-dimensional manufacturing system. *Rev. Sci. Instrum.* **2012**, *83*, 125001.
(43) Luo, J.; Niu, Z. P. Jet and Shock Wave from Collapse of Two Cavitation Bubbles. *Sci. Rep.* **2019**, *9*, 1−13.
(44) Tiong, T. J.; Chandesa, T.; Yap, Y. H. Comparison of sonochemiluminescence images using image analysis techniques and identification of acoustic pressure fields via simulation. *Ultrason. Sonochem.* **2017**, *36*, 78−87.

https://doi.org/10.1021/acsomega.1c02177
ACS Omega 2021, 6, 18281−18288